Model Analysis of Post-Stimulation Block of a Myelinated Axon by Direct Current

Jianan Jian, *Member, IEEE*, Jonathan M. Beckel, William C. de Groat, and Changfeng Tai, *Senior Member, IEEE*

Abstract*—*Objective: **To determine the role of ion concentrations and ion pump activity in conduction block of myelinated axon induced by a long-duration direct current (DC).** ***Methods:*** **A new axonal conduction model for myelinated axons based on the classical Frankenhaeuser-Huxley (FH) equations is developed that includes ion pump activity and allows the intracellular and extracellular Na^+ and K^+ concentrations to change with axonal activity.** ***Results:*** **Action potential generation, propagation, and acute DC block occurring within a short period (milliseconds) that do not significantly change the ion concentrations or trigger ion pump activity are successfully simulated by the new model in a similar way as the classical FH model. Different from the classical model, the new model also successfully simulates the post-stimulation block phenomenon, i.e., the axonal conduction block occurring after terminating a long-duration (30 seconds) DC stimulation as observed recently in animal studies. The model reveals a significant K^+ accumulation outside the axonal node as the possible mechanism underlying the post-DC block that is slowly reversed by ion pump activity during the post-stimulation period.** ***Conclusion:*** **Changes in ion concentrations and ion pump activity play an important role in post-stimulation block induced by long-duration DC stimulation.** ***Significance:*** **Long-duration stimulation is used clinically for many neuromodulation therapies, but the effects on axonal conduction/block are poorly understood. This new model will be useful for better understanding of the mechanisms underlying long-duration stimulation that changes ion concentrations and triggers ion pump activity.**

***Index Terms*—Axon, block, conduction, model, simulation.**

I. Introduction

NEUROMODULATION devices have been widely used in clinical applications for pain management and neurological disease treatment [1], [2], [3]. While the basic mechanism for action potential initiation and conduction is known, many other phenomena associated with the axonal response to neuromodulation are still not fully understood, such as post-stimulation block caused by a long-duration DC electrical stimulation [4], [5]. While classical axonal conduction models based on Hodgkin-Huxley (HH) model of unmyelinated axon or Frankenhaeuser-Huxley (FH) model of myelinated axon [6], [7], [8], [9] can successfully simulate the rise and fall of a single action potential, the change in intracellular and extracellular ion concentrations and the ion pump activity that may determine the post-stimulation effects induced by a long-duration stimulation are ignored in these classical models. Therefore, a previous study [10] using the classical FH model has failed to simulate the post-stimulation block induced by a long-duration electrical stimulation. Recently, a new axonal conduction model of unmyelinated axon that includes the changes in ion concentrations and ion pump activity has successfully simulated the post-stimulation block [11], [12]. However, a comparable model for myelinated axons is still needed since the post-stimulation block phenomenon has been observed in both unmyelinated and myelinated axons [4], [5], [13], [14]. Model analysis of the post-stimulation effect induced by a long-duration stimulation is important for understanding the possible mechanisms underlying neuromodulation therapies and developing new therapies to treat many neurological disorders [1], [2], [3].

In this study, we developed a mathematical model of nerve conduction for myelinated axons that includes the changes in intracellular and extracellular ion concentrations, the drift and diffusion currents in the axoplasm and the periaxonal space, and the cross-membrane currents including voltage-gated ion channel currents, leakage currents, and ion pump currents. Nonhomogeneous geometric parameters of myelinated axons were used in this model to reflect the actual axon properties around nodes of Ranvier [15]. This new model of myelinated axons not only successfully simulated action potential generation, conduction, and block as the classical models, but also revealed an important role of ion concentrations and ion pumps in axonal responses to long-duration electrical stimulation. This model can be used to better understand the possible mechanisms of action underlying prolonged electrical stimulation that are applied chronically to treat different neurological disorders [1], [2], [3].

II. Methods

The axonal conduction model developed in this study is shown in Fig. 1 using the same geometric parameters for myelinated

Manuscript received 12 November 2022; revised 25 December 2022, 20 January 2023, and 9 February 2023; accepted 9 February 2023. Date of publication 13 February 2023; date of current version 19 July 2023. This work was supported by the National Institute of Neurological Disorders and Stroke under Grant R01NS109198. *(Corresponding author: Changfeng Tai.)*

Jianan Jian, Jonathan M. Beckel, and William C. de Groat are with the University of Pittsburgh, USA.

Changfeng Tai is with the University of Pittsburgh, Pittsburgh, PA 15260 USA (e-mail: cftai@pitt.edu).

This article has supplementary downloadable material available at https://doi.org/10.1109/TBME.2023.3244529, provided by the authors.

Digital Object Identifier 10.1109/TBME.2023.3244529

0018-9294 © 2023 IEEE. Personal use is permitted, but republication/redistribution requires IEEE permission.
See https://www.ieee.org/publications/rights/index.html for more information.

Authorized licensed use limited to: University of Maryland College Park. Downloaded on May 07,2026 at 01:53:45 UTC from IEEE Xplore. Restrictions apply.

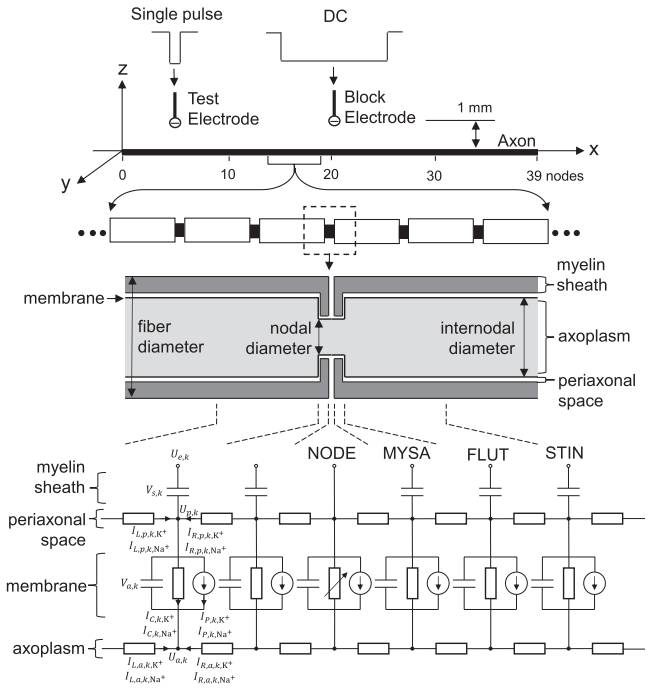

Fig. 1. Myelinated axonal model used to simulate conduction block induced by direct current (DC). The model includes 39 nodal segments and 429 internodal segments. Each segment has four layers: axoplasm, membrane, periaxonal space, and myelin sheath. Each internodal segment consists of 2 paranodal myelin attachment segments (MYSA), 2 paranodal main segments (FLUT), and 6 internodal segments (STIN). The membrane current includes voltage-gated ion channel currents (node only), leak current, ion pump current, and capacitive membrane current. The axoplasm and periaxonal space are modeled as conductors (resistors) and the myelin sheath is modeled as an isolator (capacitor).

axons as used in a previous study by McIntyre et al. [15]. The modeled axon consists of 39 nodal segments separated by myelinated segments between neighboring two nodal segments. Each myelinated segment consists of 6 internodal segments (STIN) with additional 1 paranodal main segment (FLUT) and 1 paranodal myelin attachment segment (MYSA) on each end of the myelinated segment to attach to the nodal segment (NODE) (see Fig. 1). At the two ends of the modeled axon, the myelinated segment consists of 1 MYSA, 1 FLUT, and 3 STINs with the sealed boundary conditions (no longitudinal currents). Therefore, the model has a total of 429 segments (39 nodal segments + 390 myelinated segments under the myelin sheath). The axoplasm is surrounded by axon membrane, periaxonal space, and myelin sheath (see Fig. 1). For the myelinated segment, the periaxonal space is the thin space between the membrane and the myelin sheaths. For the nodal segment, the periaxonal space is between the membrane and the perineurium. The potassium concentration $[\mathrm{K}^+]$, sodium concentration $[\mathrm{Na}^+]$, and electrical potential U in the axon are indexed at the segment k in the axoplasm by $[\mathrm{K}^+]_{a,k}, [\mathrm{Na}^+]_{a,k}, U_{a,k}$ and in the periaxonal space by $[\mathrm{K}^+]_{p,k}, [\mathrm{Na}^+]_{p,k}, U_{p,k}$.

The geometric parameters of each segment are given in Table I for an axon of fiber diameter $D_a = 10\ \mu\mathrm{m}$. These parameters are calculated from the data in Table I of a previous study by

TABLE I
GEOMETRIC PARAMETERS FOR A 10 μM DIAMETER FIBER

Segment k	NODE	MYSA	FLUT	STIN
Length $L_{a,k}(\mu\mathrm{m})$ [15]	1	3	46	175.2
Diameter $(\mu\mathrm{m})$ [15]	3.3	3.3	6.9	6.9
Periaxonal space width $(\mu\mathrm{m})$ [15]	N/A	0.002	0.004	0.004
Axoplasm cross-section $A_{a,k}(\mu\mathrm{m}^2)$	8.553	8.553	37.39	37.39
Periaxonal space cross-section $A_{p,k}(\mu\mathrm{m}^2)$	69.99	0.02073	0.08671	0.08671
Membrane surface area $S_k(\mu\mathrm{m}^2)$	10.37	31.10	997.1	3798
Axoplasm volume $\Gamma_{a,k}(\mu\mathrm{m}^3)$	8.553	25.66	1720	6551
Periaxonal space volume $\Gamma_{p,k}(\mu\mathrm{m}^3)$	1885	0.06219	3.989	15.19

TABLE II
MEMBRANE PERMEABILITY AND ELECTRICAL PARAMETERS

Segment k	NODE	MYSA	FLUT	STIN
Leak conductance at resting potential g $(\mathrm{S/cm}^2)$ [15]	0.007	0.001	0.0001	0.0001
K^+ leak permeability $P_{l\mathrm{K}^+,k}(\mathrm{cm/s})$	6.158e-5	8.797e-6	8.797e-7	8.797e-7
Na^+ leak permeability $P_{l\mathrm{Na}^+,k}(\mathrm{cm/s})$	4.108e-6	5.807e-7	5.807e-8	5.807e-8
Membrane capacitance $(\mu\mathrm{F/cm}^2)$ [15]	2	2	2	2
Myelin capacitance $(\mu\mathrm{F/cm}^2)$ [15]	NA	0.1	0.1	0.1
Pump coefficient $a_k(\mu\mathrm{A/cm}^2)$	0.5483	0.0783	0.0078	0.0078

McIntyre et al. [15] except for the periaxonal space volume $\Gamma_{p,k}$ at the nodal segment. We assume that the periaxonal space at the nodal segment consists of two parts. The first part is the narrow space between the membrane and the endoneurium within the outer boundary of the myelin sheaths (see Fig. 1). The volume of the first part is $(\frac{\pi}{4}D_a^2 - A_{a,k})L_{a,k} = 70\ \mu\mathrm{m}^3$. The second part is a thin peri-myelin space covering the myelin sheath extending from one node to the next and surrounded by perineurium. The internodal distance is $L = 1.15$ mm for a 10-μm diameter fiber. Assuming the thickness of this thin peri-myelin space is $\eta = 0.5\%$ of the fiber diameter, then the volume of the second part is $((1+2\eta)^2 - 1)\frac{\pi}{4}D_a^2 L = 1815\ \mu\mathrm{m}^3$. Therefore, the total volume of the periaxonal space at the nodal segment is $\Gamma_{p,k} = 1885\ \mu\mathrm{m}^3$. The geometric parameters for different diameter axons can be calculated similarly using previously published data by McIntyre et al. [15]. The membrane permeability and electrical parameters for each segment are listed in Table II.

The ion concentration gradient ∇c causes a diffusion flux J , given by Fick's law $J = -D\nabla c$. The constant D is the diffusion coefficient. $D_{\mathrm{K}^+} = 1.957 \times 10^{-5}\mathrm{cm}^2/\mathrm{s}$ and $D_{\mathrm{Na}^+} =$

Authorized licensed use limited to: University of Maryland College Park. Downloaded on May 07,2026 at 01:53:45 UTC from IEEE Xplore. Restrictions apply.

TABLE III
OTHER MODEL PARAMETERS

Initial extracellular Na^+ concentration (mM) [9]	114.5	K^+ diffusion coefficient $D_{K^+}(cm^2/s)$ [16]	1.957e-5
Initial extracellular K^+ concentration (mM) [9]	2.5	Na^+ diffusion coefficient $D_{Na^+}(cm^2/s)$ [16]	1.334e-5
Initial intracellular Na^+ concentration (mM) [9]	13.74	Pump parameter b_1(mM) [17]	1
Initial intracellular K^+ concentration (mM) [9]	120	Pump parameter b_2(mM) [17]	30
K^+ channel maximum permeability $P_s(\mathrm{cm}/s)$ [9]	1.2e-3	Pump parameter $c(1/\mathrm{mM})$ [17]	0.05
Fast Na^+ channel maximum permeability $P_f(\mathrm{cm}/s)$ [9]	8e-3	Pump parameter d	0.813
Persistent Na^+ channel maximum permeability $P_p(\mathrm{cm}/s)$ [9]	0.54e-3	Initial fast Na^+ activation variable m	0.0005
Extracellular resistivity $\rho_e(\Omega\mathrm{cm})$	300	Initial fast Na^+ inactivation variable h	0.8249
Resting potential (mV) [9]	-70	Initial persistent Na^+ activation variable p	0.0049
Temperature T(K) [9]	293	Initial K^+ activation variable n	0.0268

$1.334 \times 10^{-5}\mathrm{cm}^2/\mathrm{s}$ [16] to follow other parameters also obtained at room temperature (see Table III). Electrical field E is the negative of the electrical potential gradient $E = -\nabla U$. It causes a drift flux given by $J = cv$, where the drift velocity v is given by $v = \mu E$. The constant of proportionality μ is called the electrical mobility. The diffusion coefficient D and the electrical mobility μ satisfy the Einstein relation $D = \mu kT/ze$, where T is the temperature which is set at $20^\circ C = 293\mathrm{K}$ in this study, z is the ion charge ($z_{\mathrm{K}^+} = z_{\mathrm{Na}^+} = +1$), k is the Boltzmann constant, and e is the elementary charge. The Boltzmann constant k is related to the gas constant R by the Avogadro constant $k = R/N_{\mathrm{A}}$. Similarly, the elementary charge e is related to the Faraday constant F by the Avogadro constant $e = F/N_{\mathrm{A}}$. The total flux is the sum of the diffusion flux and the drift flux, and can be written as [17]

$$J = -D\nabla c + cv = -D\nabla c - c\mu\nabla U = -D\nabla c - c\frac{zeD}{kT}\nabla U$$
$$= -D\left(\nabla c + \frac{ze}{kT}c\nabla U\right) = -D\left(\nabla c + \frac{zF}{RT}c\nabla U\right) \quad (1)$$

Ionic flux J can be converted to electrical current I by multiplying with the amount of charge per mole of ions zF and the cross-sectional area A. We obtain

$$I = zFAJ = -zFAD\left(\nabla c + \frac{zF}{RT}c\nabla U\right) \quad (2)$$

We can discretize (2) to describe the longitudinal currents between two adjacent segments within the periaxonal space or within the axoplasm. Let U_k, c_k be the potential and the ion concentration at the segment k. Let U_B, c_B be the potential and the ion concentration at the boundary that separates the longitudinal resistor into 2 parts belonging to segment k and segment $k+1$ respectively, i.e., the boundary is within the longitudinal resistor that connects segment k and segment k+1. We assume that the function U is linear between U_k and U_B and the function c is linear between c_k and c_B. Then based on (2) the longitudinal current on the left side of the boundary is

$$I_{B^-} = -zFA_kD\left(\frac{c_B - c_k}{L_k/2} + \frac{zF}{RT}c_B\frac{U_B - U_k}{L_k/2}\right)$$

and the longitudinal current on the right side of the boundary is

$$I_{B^+} = -zFA_{k+1}D\left(\frac{c_{k+1} - c_B}{L_{k+1}/2} + \frac{zF}{RT}c_B\frac{U_{k+1} - U_B}{L_{k+1}/2}\right)$$

Since the longitudinal current is continuous across the boundary $I_{B^-} = I_{B^+}$, then

$$\frac{A_k}{L_k}\left((c_B - c_k) + \frac{zF}{RT}c_B\left(U_B - U_k\right)\right)$$
$$= \frac{A_{k+1}}{L_{k+1}}\left((c_{k+1} - c_B) + \frac{zF}{RT}c_B\left(U_{k+1} - U_B\right)\right)$$

Since this should be true if c is constant, i.e., $c_k = c_B = c_{k+1}$, then

$$U_B = \frac{\frac{A_k}{L_k}U_k + \frac{A_{k+1}}{L_{k+1}}U_{k+1}}{\frac{A_k}{L_k} + \frac{A_{k+1}}{L_{k+1}}} \quad and \quad c_B = \frac{\frac{A_k}{L_k}c_k + \frac{A_{k+1}}{L_{k+1}}c_{k+1}}{\frac{A_k}{L_k} + \frac{A_{k+1}}{L_{k+1}}}$$

Letting $\lambda_k = A_k/L_k$ and replacing U_B, c_B with above equations, we obtain

$$I_{B^-} = I_{B^+} = -2zFD\frac{\lambda_k\lambda_{k+1}}{\lambda_k + \lambda_{k+1}}\Bigg((c_{k+1} - c_k)$$
$$+ \frac{zF}{RT}\frac{\lambda_k c_k + \lambda_{k+1}c_{k+1}}{\lambda_k + \lambda_{k+1}}\left(U_{k+1} - U_k\right)\Bigg)$$

Therefore, the longitudinal currents from segment $k+1$ to segment k as shown in Fig. 1 can be written as follows:

$$I_{R,a,k,\mathrm{K}^+} = 2FD_{\mathrm{K}^+}\frac{\lambda_{a,k}\lambda_{a,k+1}}{\lambda_{a,k} + \lambda_{a,k+1}}\Bigg(\left(\left[\mathrm{K}^+\right]_{a,k+1} - \left[\mathrm{K}^+\right]_{a,k}\right)$$
$$+ \frac{F}{RT}\frac{\lambda_{a,k+1}[\mathrm{K}^+]_{a,k+1} + \lambda_{a,k}[\mathrm{K}^+]_{a,k}}{\lambda_{a,k+1} + \lambda_{a,k}}\left(U_{a,k+1} - U_{a,k}\right)\Bigg)$$

$$I_{R,a,k,\mathrm{Na}^+} = 2FD_{\mathrm{Na}^+}\frac{\lambda_{a,k}\lambda_{a,k+1}}{\lambda_{a,k} + \lambda_{a,k+1}}\Bigg(\left(\left[\mathrm{Na}^+\right]_{a,k+1} - \left[\mathrm{Na}^+\right]_{a,k}\right)$$
$$+ \frac{F}{RT}\frac{\lambda_{a,k+1}[\mathrm{Na}^+]_{a,k+1} + \lambda_{a,k}[\mathrm{Na}^+]_{a,k}}{\lambda_{a,k+1} + \lambda_{a,k}}\left(U_{a,k+1} - U_{a,k}\right)\Bigg)$$

$$I_{R,p,k,\mathrm{K}^+} = 2FD_{\mathrm{K}^+}\frac{\lambda_{p,k}\lambda_{p,k+1}}{\lambda_{p,k} + \lambda_{p,k+1}}\Bigg(\left(\left[\mathrm{K}^+\right]_{p,k+1} - \left[\mathrm{K}^+\right]_{p,k}\right)$$
$$+ \frac{F}{RT}\frac{\lambda_{p,k+1}[\mathrm{K}^+]_{p,k+1} + \lambda_{p,k}[\mathrm{K}^+]_{p,k}}{\lambda_{p,k+1} + \lambda_{p,k}}\left(U_{p,k+1} - U_{p,k}\right)\Bigg)$$

$$I_{R,p,k,\mathrm{Na}^+} = 2FD_{\mathrm{Na}^+}\frac{\lambda_{p,k}\lambda_{p,k+1}}{\lambda_{p,k} + \lambda_{p,k+1}}\Bigg(\left(\left[\mathrm{Na}^+\right]_{p,k+1} - \left[\mathrm{Na}^+\right]_{p,k}\right)$$

Authorized licensed use limited to: University of Maryland College Park. Downloaded on May 07,2026 at 01:53:45 UTC from IEEE Xplore. Restrictions apply.

$$+\frac{F}{RT}\frac{\lambda_{p,k+1}[\mathrm{Na}^+]_{p,k+1}+\lambda_{p,k}[\mathrm{Na}^+]_{p,k}}{\lambda_{p,k+1}+\lambda_{p,k}}\left(U_{p,k+1}-U_{p,k}\right)\Bigg)$$

By symmetry, the currents from segment $k-1$ to segment k are:

$$I_{L,a,k,\mathrm{K}^+} = -I_{R,a,k-1,\mathrm{K}^+}$$
$$I_{L,a,k,\mathrm{Na}^+} = -I_{R,a,k-1,\mathrm{Na}^+}$$
$$I_{L,p,k,\mathrm{K}^+} = -I_{R,p,k-1,\mathrm{K}^+}$$
$$I_{L,p,k,\mathrm{Na}^+} = -I_{R,p,k-1,\mathrm{Na}^+}$$

The sealed boundary conditions are implemented by $I_{L,a,k,\mathrm{K}^+} = I_{L,a,k,\mathrm{Na}^+} = I_{L,p,k,\mathrm{K}^+} = I_{L,p,k,\mathrm{Na}^+} = 0$ for $k = 1$ and $I_{R,a,k,\mathrm{K}^+} = I_{R,a,k,\mathrm{Na}^+} = I_{R,p,k,\mathrm{K}^+} = I_{R,p,k,\mathrm{Na}^+} = 0$ for $k = 429$.

The currents across the axonal membrane at the segment k generated by Na^+-K^+-pumps (I_{P,k,Na^+} and I_{P,k,K^+}) are calculated by:

$$I_{P,k,\mathrm{K}^+} = a_k\left(1+b_1/\left[\mathrm{K}^+\right]_{p,k}\right)^{-2}\left(1+b_2/\left[\mathrm{Na}^+\right]_{a,k}\right)^{-1}$$
$$I_{P,k,\mathrm{Na}^+} = -\left(d+c\left[\mathrm{Na}^+\right]_{a,k}\right)I_{P,k,\mathrm{K}^+}$$

where a_k is a constant that we calculated so that the total net current at the resting state is zero (see Table II), d is a constant such that $I_{P,k,\mathrm{Na}^+}/I_{P,k,\mathrm{K}^+} = -1.5$ at the resting state, and $b_1 = 1$ mM, $b_2 = 30$ mM, $c = 0.05$ (see Table III) [18].

To derive the ion channel currents across axonal membrane at the segment k, we assume that the membrane thickness W is much smaller than the axon radius r, i.e., $W \ll r$ and we ignore any boundary effect. Let y be the coordinate perpendicular to the membrane, the ion concentration c is a function of y coordinate alone, ionic flux J is a constant, and $\nabla = d/dy$. Let $y = 0$ be the inside surface of the membrane and $y = W$ the outside surface of the membrane. Consider the boundary conditions $c(0) = c_i, c(W) = c_o, U(0) - U(W) = V_a$ and assume the electrical field $E = -\nabla U = V_a/W$ within the membrane is constant. Then, equation (1) becomes a linear ordinary differential equation:

$$\frac{d}{dy}c(y) - \frac{zF}{RT}\frac{V_a}{W}c(y) = -\frac{J}{D}$$

The following solution satisfies this differential equation:

$$c_o = \left(c_i - \frac{RTJW}{zFV_aD}\right)\exp\left(\frac{zFV_a}{RT}\right) + \frac{RTJW}{zFV_aD}$$

Since the membrane permeability $P = D/W$ and rearranging the equation above, we have

$$J = P\frac{zFV_a}{RT}\frac{c_i\exp\left(zFV_a/RT\right) - c_o}{\exp\left(zFV_a/RT\right)-1}$$

The ionic flux can be converted to electrical current by $I = zFSJ$ where S represents the membrane surface area, and we have

$$I = PS\frac{z^2F^2V_a}{RT}\frac{c_i\exp\left(zFV_a/RT\right) - c_o}{\exp\left(zFV_a/RT\right)-1} \tag{3}$$

Denote the cross-membrane potential at the segment k by $V_{a,k} = U_{a,k} - U_{p,k}$. We have the cross-membrane ionic currents for potassium (I_{C,k,K^+}) and sodium (I_{C,k,Na^+}) channels as follows:

$$I_{C,k,\mathrm{K}^+} = -P_{\mathrm{K}^+,k}S_k\frac{F^2V_{a,k}}{RT} \times \frac{\left[\mathrm{K}^+\right]_{a,k}\exp\left(FV_{a,k}/RT\right) - \left[\mathrm{K}^+\right]_{p,k}}{\exp\left(FV_{a,k}/RT\right)-1}$$

$$I_{C,k,\mathrm{Na}^+} = -P_{\mathrm{Na}^+,k}S_k\frac{F^2V_{a,k}}{RT} \times \frac{\left[\mathrm{Na}^+\right]_{a,k}\exp\left(FV_{a,k}/RT\right) - \left[\mathrm{Na}^+\right]_{p,k}}{\exp\left(FV_{a,k}/RT\right)-1}$$

where the S_k is the membrane surface area at the segment k.

The ion channels in the axonal segments underneath the myelin are not voltage gated. The membrane permeabilities for potassium ($P_{\mathrm{K}^+,k}$) and sodium ($P_{\mathrm{Na}^+,k}$) at these myelinated segments are solely constant leak permeabilities $P_{\mathrm{Na}^+,k} = P_{l\mathrm{Na}^+,k}$ and $P_{\mathrm{K}^+,k} = P_{l\mathrm{K}^+,k}$. The values of leak permeabilities given in Table II are calculated by converting membrane conductance used in a previous study [15] into permeabilities using the following equations. Based on (3), the potassium and sodium currents per unit area are given by the constant field equations:

$$I_{\mathrm{K}^+} = P_{\mathrm{K}^+}\frac{F^2}{RT}\frac{V}{e^{\frac{FV}{RT}}-1}\left(\left[\mathrm{K}^+\right]_a e^{\frac{FV}{RT}} - \left[\mathrm{K}^+\right]_p\right)$$

$$I_{\mathrm{Na}^+} = P_{\mathrm{Na}^+}\frac{F^2}{RT}\frac{V}{e^{\frac{FV}{RT}}-1}\left(\left[\mathrm{Na}^+\right]_a e^{\frac{FV}{RT}} - \left[\mathrm{Na}^+\right]_p\right)$$

The membrane conductance g can be calculated by:

$$g = \frac{\partial}{\partial V}\left(I_{\mathrm{K}^+} + I_{\mathrm{Na}^+}\right) = \frac{F^2}{RT}\Bigg(\frac{X_ae^v - X_p}{e^v-1} + \frac{ve^v}{\left(e^v-1\right)^2}\left(X_p - X_a\right)\Bigg)$$

where $v = FV/RT$, $X_a = P_{\mathrm{K}^+}[\mathrm{K}^+]_a + P_{\mathrm{Na}^+}[\mathrm{Na}^+]_a$, and $X_p = P_{\mathrm{K}^+}[\mathrm{K}^+]_p + P_{\mathrm{Na}^+}[\mathrm{Na}^+]_p$. At the equilibrium membrane potential given by the Goldman equation

$$V = \frac{RT}{F}\ln\frac{P_{\mathrm{K}^+}\left[\mathrm{K}^+\right]_p + P_{\mathrm{Na}^+}\left[\mathrm{Na}^+\right]_p}{P_{\mathrm{K}^+}\left[\mathrm{K}^+\right]_a + P_{\mathrm{Na}^+}\left[\mathrm{Na}^+\right]_a} = \frac{RT}{F}\ln\frac{X_p}{X_a}$$

then

$$v = \frac{FV}{RT} = \ln\frac{X_p}{X_a}$$
$$e^v = \frac{X_p}{X_a}$$

and the membrane conductance g becomes

$$g = \frac{F^2}{RT}\frac{v}{e^v-1}X_p = \frac{F^3}{R^2T^2}\frac{V}{e^{\frac{FV}{RT}}-1} \times \left(P_{\mathrm{K}^+}\left[\mathrm{K}^+\right]_p + P_{\mathrm{Na}^+}\left[\mathrm{Na}^+\right]_p\right)$$

Authorized licensed use limited to: University of Maryland College Park. Downloaded on May 07,2026 at 01:53:45 UTC from IEEE Xplore. Restrictions apply.

Let $\eta = P_{\mathrm{Na}^+} / P_{\mathrm{K}^+}$ then we obtain

$$P_{\mathrm{K}^+} = \frac{R^2T^2\left(e^{\frac{FV}{RT}} - 1\right)}{F^3V\left([\mathrm{K}^+]_p + \eta[\mathrm{Na}^+]_p\right)}g$$

We make the approximation that $V \approx V_r = -70$ mV where V_r follows the modified Goldman equation

$$V_r = \frac{RT}{F}\ln\frac{1.5P_{\mathrm{K}^+}[\mathrm{K}^+]_p + P_{\mathrm{Na}^+}[\mathrm{Na}^+]_p}{1.5P_{\mathrm{K}^+}[\mathrm{K}^+]_a + P_{\mathrm{Na}^+}[\mathrm{Na}^+]_a}$$

from which we obtain the value of η

$$\eta = \frac{P_{\mathrm{Na}^+}}{P_{\mathrm{K}^+}} = -1.5\frac{[\mathrm{K}^+]_a e^{\frac{FV_r}{RT}} - [\mathrm{K}^+]_p}{[\mathrm{Na}^+]_a e^{\frac{FV_r}{RT}} - [\mathrm{Na}^+]_p}.$$

Using the initial Na^+ and K^+ concentrations given in Table III, we obtain $\eta = 0.06601$. In myelinated segments, the leak permeabilities $P_{l\mathrm{Na}^+,k}, P_{l\mathrm{K}^+,k}$ are simply the resting state permeabilities $P_{\mathrm{K}^+}, P_{\mathrm{Na}^+}$. In nodal segments, the leak permeabilities are $P_{l\mathrm{Na}^+,k} = P_{\mathrm{Na}^+} - P_f m_k^2 h_k - P_p p_k^2$ and $P_{l\mathrm{K}^+,k} = P_{\mathrm{K}^+} - P_s n_k^2$ where m_k, h_k, p_k, n_k have the initial values given in Table III.

In the nodal segment k, the membrane permeabilities are also determined by the voltage-gated channels, i.e., $P_{\mathrm{Na}^+,k} = P_{l\mathrm{Na}^+,k} + P_f m_k^2 h_k + P_p p_k^2$ and $P_{\mathrm{K}^+,k} = P_{l\mathrm{K}^+,k} + P_s n_k^2$ where the P_f, P_p, and P_s are the maximal permeabilities for fast Na^+ channels, persistent Na^+ channels, and K^+ channel, respectively (see Table III). The fast Na^+ channel activation variable m, fast Na^+ channel inactivation variable h, persistent Na^+ channel activation variable p, and K^+ channel activation variable n follow the first-order kinetics controlled by depolarization $V_k = V_{a,k} - V_r$ where $V_r = -70$ mV is the resting potential [6], [9]:

$$\frac{dm}{dt} = \alpha_m(1-m) + \beta_m m \qquad \frac{dh}{dt} = \alpha_h(1-h) + \beta_h h$$

$$\frac{dp}{dt} = \alpha_p(1-p) + \beta_p p \qquad \frac{dn}{dt} = \alpha_n(1-n) + \beta_n n$$

$$\alpha_m = \frac{0.36(V_k - 22)}{1 - \exp\left(\frac{22-V_k}{3}\right)}1.8^{(T-293)/10}$$

$$\beta_m = \frac{0.4(13 - V_k)}{1 - \exp\left(\frac{V_k-13}{20}\right)}1.8^{(T-293)/10}$$

$$\alpha_h = \frac{-0.1(V_k + 10)}{1 - \exp\left(\frac{V_k+10}{6}\right)}3^{(T-293)/10}$$

$$\beta_h = \frac{4.5}{1 + \exp\left(\frac{45-V_k}{10}\right)}3^{(T-293)/10}$$

$$\alpha_p = \frac{0.006(V_k - 40)}{1 - \exp\left(\frac{40-V_k}{10}\right)}3^{(T-293)/10}$$

$$\beta_p = \frac{-0.09(V_k + 25)}{1 - \exp\left(\frac{V_k+25}{20}\right)}3^{(T-293)/10}$$

$$\alpha_n = \frac{0.02(V_k - 35)}{1 - \exp\left(\frac{35-V_k}{10}\right)}3^{(T-293)/10}$$

$$\beta_n = \frac{0.05(10 - V_k)}{1 - \exp\left(\frac{V_k-10}{10}\right)}3^{(T-293)/10}$$

The changes of sodium and potassium concentrations are described by the following equations:

$$\frac{d[\mathrm{K}^+]_{a,k}}{dt} = \frac{1}{\Gamma_{a,k}F} \times \left(I_{L,a,k,\mathrm{K}^+} + I_{R,a,k,\mathrm{K}^+} + I_{C,k,\mathrm{K}^+} + I_{P,k,\mathrm{K}^+}\right)$$

$$\frac{d[\mathrm{Na}^+]_{a,k}}{dt} = \frac{1}{\Gamma_{a,k}F} \times \left(I_{L,a,k,\mathrm{Na}^+} + I_{R,a,k,\mathrm{Na}^+} + I_{C,k,\mathrm{Na}^+} + I_{P,k,\mathrm{Na}^+}\right)$$

$$\frac{d[\mathrm{K}^+]_{p,k}}{dt} = \frac{1}{\Gamma_{p,k}F} \times \left(I_{L,p,k,\mathrm{K}^+} + I_{R,p,k,\mathrm{K}^+} - I_{C,k,\mathrm{K}^+} - I_{P,k,\mathrm{K}^+}\right)$$

$$\frac{d[\mathrm{Na}^+]_{p,k}}{dt} = \frac{1}{\Gamma_{p,k}F} \times \left(I_{L,p,k,\mathrm{Na}^+} + I_{R,p,k,\mathrm{Na}^+} - I_{C,k,\mathrm{Na}^+} - I_{P,k,\mathrm{Na}^+}\right)$$

where $\Gamma_{a,k}$ and $\Gamma_{p,k}$ are the axoplasm volume and periaxonal space volume of each segment given in Table I.

We assume that the axon is in an infinite homogeneous medium (resistivity $\rho_e = 300\ \Omega$cm). After neglecting the small influence of the axon in the homogeneous medium, the extracellular potential $U_{e,k}$ at the segment k along the axon can be calculated by:

$$U_{e,k} = \frac{\rho_e}{4\pi}\left(\frac{I_{\text{block}}(t)}{\sqrt{(x_k - x_{\text{block}})^2 + z_0^2}} + \frac{I_{\text{test}}(t)}{\sqrt{(x_k - x_{\text{test}})^2 + z_0^2}}\right)$$

where $I_{\text{block}}(t)$ is the DC stimulation delivered to the block electrode; $I_{\text{test}}(t)$ is the single test pulse delivered to the test electrode. x_k is the longitudinal coordinate of segment k, x_{block} and x_{test} are the longitudinal coordinates of the stimulation electrodes that are positioned $z_0 = 1$ mm away from the axon (see Fig. 1).

The cross-membrane potential $V_{a,k} = U_{a,k} - U_{p,k}$ and the potential across the myelin sheath $V_{s,k} = U_{p,k} - U_{e,k}$ (see Fig. 1) are described by:

$$\frac{dV_{a,k}}{dt} = \frac{1}{C_{a,k}}\left(I_{L,a,k,\mathrm{K}^+} + I_{R,a,k,\mathrm{K}^+} + I_{C,k,\mathrm{K}^+} + I_{P,k,\mathrm{K}^+} + I_{L,a,k,\mathrm{Na}^+} + I_{R,a,k,\mathrm{Na}^+} + I_{C,k,\mathrm{Na}^+} + I_{P,k,\mathrm{Na}^+}\right)$$

$$\frac{dV_{s,k}}{dt} = \frac{1}{C_{s,k}}\left(I_{L,a,k,\mathrm{K}^+} + I_{R,a,k,\mathrm{K}^+} + I_{L,p,k,\mathrm{K}^+} + I_{R,p,k,\mathrm{K}^+} + I_{L,a,k,\mathrm{Na}^+} + I_{R,a,k,\mathrm{Na}^+} + I_{L,p,k,\mathrm{Na}^+} + I_{R,p,k,\mathrm{Na}^+}\right)$$

The total capacitance at nodal segments is $C_{a,k} = S_k \times 2\ \mu\mathrm{F/cm}^2$ and at the myelin segment the total capacitance is $C_{s,k} = S_k/240 \times 0.1\ \mu\mathrm{F/cm}^2$ [15] (Table I).

The initial intracellular and extracellular sodium and potassium concentrations of the axon are same as the original FH model [9] (see Table III). The simulation is carried out using MATLAB with the ode15s solver.

Authorized licensed use limited to: University of Maryland College Park. Downloaded on May 07,2026 at 01:53:45 UTC from IEEE Xplore. Restrictions apply.

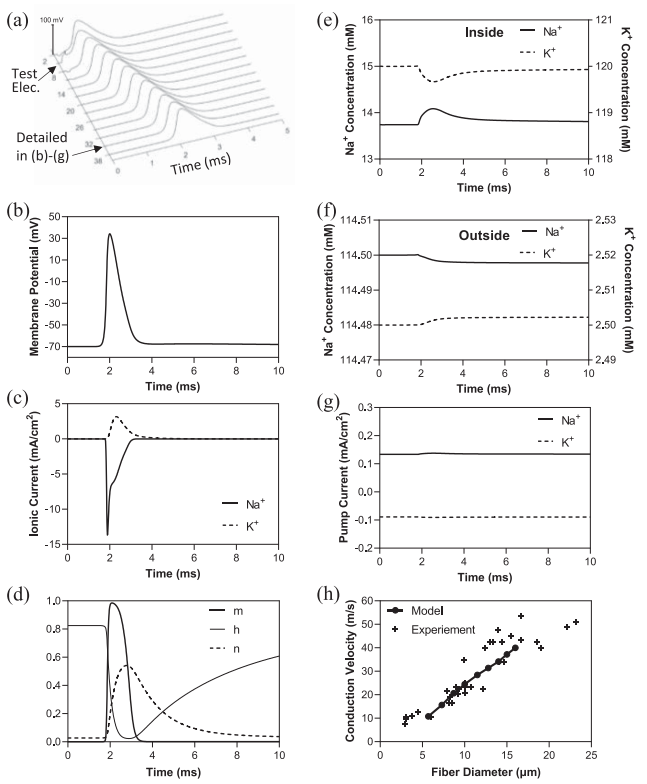

Fig. 2. Action potential generation and conduction. (a) Propagation of an action potential induced by a test pulse (0.32 mA, 0.1 ms) applied from a point source 1 mm away from the node 5 on an axon of 10 μm fiber diameter (see Fig. 1). (b)-(g). Detailed presentations of the membrane potential (b), ionic currents (c), activation and inactivation of Na^+ and K^+ channels (d), ion concentrations inside (e) and outside (f) the axon, and ion pump currents (g) at the node 35 as indicated by the arrow in (a). (h). Conduction velocity for axons of different diameters calculated from the model in comparison with the experimental measurements [19]. m: Na^+ channel activation; h: Na^+ channel inactivation; n: K^+ channel activation.

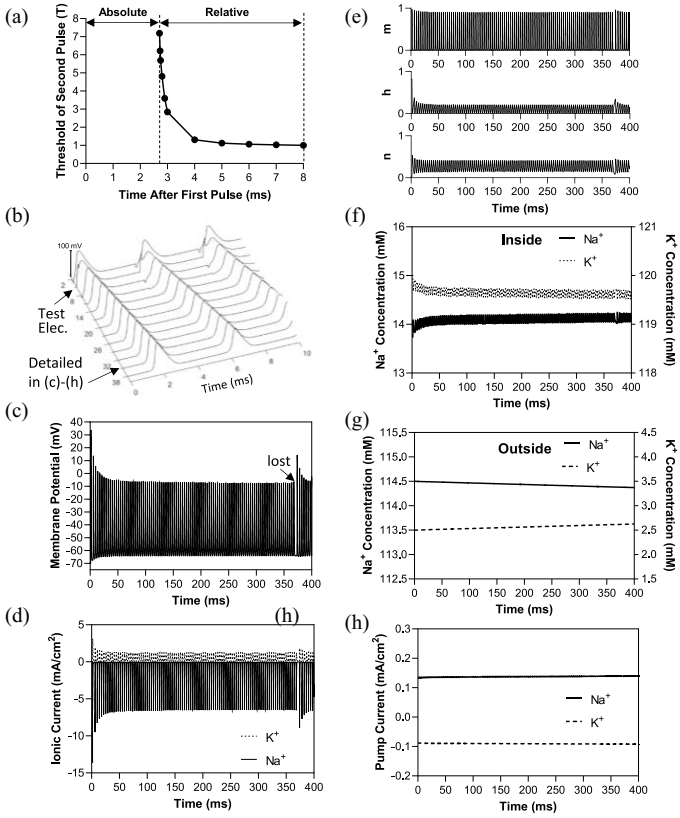

Fig. 3. Refractory period and firing frequency for a myelinated axon of 10-μm fiber diameter. (a) Absolute (2.7 ms) and relative (2.7-8 ms) refractory periods determined by double test pulses (0.1 ms). The excitation threshold (T) for the first pulse is 0.32 mA. (b). Repeated firing induced by high frequency stimulation (269 Hz, 0.1 ms) at intensity of 0.64 mA (2T). (c)-(h). Detailed representations of the membrane potential (c), ionic currents (d), activation and inactivation of Na^+ and K^+ channels (e), ion concentrations of Na^+ and K^+ inside (f) and outside (g) the axon, and ion pump currents (h) at the node 35 as indicated by the arrow in (b). m: Na^+ channel activation; h: Na^+ channel inactivation; n: K^+ channel activation.

III. Results

A. Action Potential Generation and Conduction

Using this newly developed model, action potential is successfully generated and propagates along a myelinated nerve fiber of 10-μm diameter (Fig. 2). Fig. 2(a) shows an action potential initiated by a test pulse (0.32 mA, 0.1 ms) at the node 5 propagates in both directions along the 44.85-mm long axon (39 nodes x 1.15 mm internodal distance). Fig. 2(b)-(g) present the detailed time course of this action potential at the node 35. The action potential (Fig. 2(b)), the Na^+ and K^+ ionic currents (Fig. 2(c)), and activation/inactivation of Na^+ and K^+ channels (Fig. 2(d)) are similar to the results produced by classical FH models [6], [7], [9]. The single action potential only produces minimal changes in Na^+ and K^+ concentrations inside (Fig. 2(e)) and outside (Fig. 2(f)) the axonal node. The Na^+ and K^+ pumps are not activated (Fig. 2(g)) due to the small changes in Na^+ and K^+ concentrations. The axonal conduction velocity calculated by this new model for different diameter fibers (5-15 μm) agrees very well with the experimental measurements [19] (see Fig. 2(h)).

B. Refractory Period and Firing Frequency

The refractory period is determined by applying double test pulses of 0.1 ms pulse width to a myelinated nerve fiber of 10-μm diameter. The excitation threshold (T) for the first test pulse is 0.32 mA. The absolute refractory period is 2.7 ms and the relative refractory period extends from 2.7 ms to 8 ms (Fig. 3(a)).

A 400 msec train of high frequency (269 Hz) stimulus pulses (0.1 ms) at a suprathreshold intensity (2T = 0.64 mA) can generate action potentials in response to every stimulus pulse only at the beginning of the stimulation (see Fig. 3(b)). However, as the stimulation continues one action potential is lost at 368 ms (Fig. 3(c)). However, at 268 Hz every stimulus pulse can generate an action potential during the entire 400 msec. Therefore, the highest firing frequency during a 400-ms testing period is 268 Hz with an inter-pulse interval of 3.7 ms that is very close to the relative refractory period of 3.6 ms for 2T pulses (Fig. 3(a)).

After the initial action potential that depolarizes the membrane from −70 mV to 34 mV (Fig. 2(b)), the peak depolarization gradually declines with time and stabilizes at −5 mV after 50 ms stimulation (Fig. 3(c)). This reduction in the

Authorized licensed use limited to: University of Maryland College Park. Downloaded on May 07,2026 at 01:53:45 UTC from IEEE Xplore. Restrictions apply.

maximal depolarization of an action potential is due to the partial inactivation of the Na^+ channel (Fig. 3(e)), the partial activation of K^+ channel (Fig. 3(e)), and an initial quick increase in Na^+ concentration inside the axon (Fig. 3(f)). These initial changes caused by repetitive firing gradually reduced the Na^+ current (Fig. 3(d)) that causes the reduction in peak depolarization of an action potentials (Fig. 3(c)). Meanwhile, the resting potential also gradually changes from −70 mV to −64 mV during the first 50-ms stimulation (Fig. 3(c)), which is mainly due to the initial small decrease in K^+ concentration inside the axon (Fig. 3(f)) since the ion concentrations outside the axon only change minimally (Fig. 3(g)). The effect of Na^+ concentration change on resting potential is minimal. The 269 Hz firing during a short period of 400 ms only produces very small changes in the ion concentrations both inside and outside the axon, which does not activate the ion pump activity (Fig. 3(h)).

C. Post-Stimulation Block by Direct Current (DC)

Application of DC (1.125 mA) at the node 20 of a 10-μm diameter fiber produces a large depolarization decreasing the membrane potential from the resting potential -70 mV to 10-30 mV during the 30-secs stimulation (Fig. 4(a)). This large DC depolarization results in an inactivation of fast Na^+ channel (Fig. 4(d)) and an activation of K^+ channel (Fig. 4(e)), thereby inducing a large outward K^+ current and a small inward Na^+ current (Fig. 4(b)). The large outward K^+ current significantly increases the K^+ concentration outside the axonal node to >200 mM at the end of the 30-secs DC (Fig. 4(f)) and decreases the K^+ concentration inside the axonal node (Fig. 4(h)). The small inward Na^+ current, which mainly consists of the persistent Na^+ current, slightly decreases the outside Na^+ concentration (Fig. 4(g)) and increases the inside Na^+ concentration (Fig. 4(i)). Mainly due to the large change in outside K^+ concentration, the ion pumps are activated to slowly pump Na^+ out and move K^+ back into the axon (Fig. 4(j)).

After terminating the 30-secs DC stimulation, the large depolarization is gradually reduced during the period of 30-60 seconds (between the 2 dashed lines in Fig. 4(a)) while maintaining the K^+ channel largely open during this period (Fig. 4(e)). This allows a large inward K^+ current (Fig. 4(b)) to gradually reduce the high K^+ concentration outside the axon (Fig. 4(f)) and increases the K^+ concentration inside (Fig. 4(h)). Although the large depolarization during the 30-60 sec period further reduces the Na^+ concentration outside (Fig. 4(g)) by moving Na^+ into the axon (Fig. 4(b)), the increased Na^+ concentration inside already starts to decrease even during the 30-secs stimulation (Fig. 4(i)) by diffusing into the neighboring axonal segments underneath the myelin. During the period of 60-300 secs, the membrane potential slowly recovers to the resting potential -70 mV as the ion pumps (Fig. 4(j)) are slowly pumping the K^+ back into the axon (Fig. 4(f) and (h)) and moving the Na^+ out of the axon (Fig. 4(g) and (i)). It is worth noting that at 60 secs the rate of decline of the outside K^+ concentration is changed abruptly (Fig. 4(f)). This is because the membrane potential (Fig. 4(a)) has recovered to a level that can close both Na^+ (Fig. 4(c)) and K^+ (Fig. 4(e)) channels and completely turn off

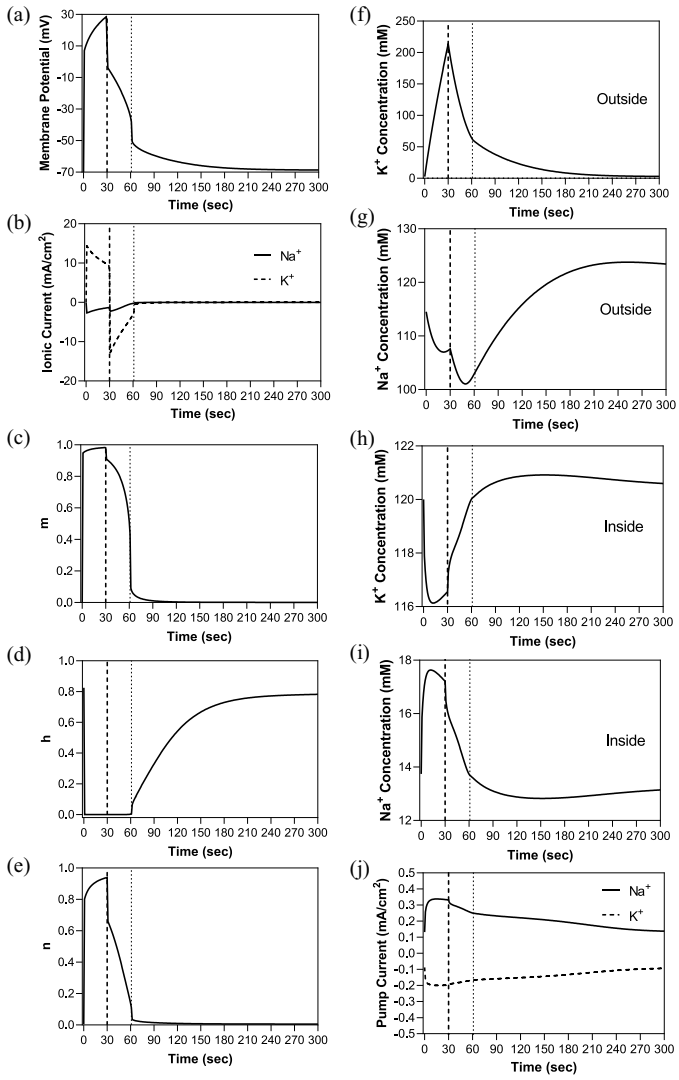

Fig. 4. DC stimulation (1.125 mA) is applied for 30 secs (thick dashed line) at node 20 of a 10-μm fiber diameter myelinated axon. Post-stimulation block at node 20 is observed from 30 to 61 secs (thin dashed line). (a)-(j). Time evolution at node 20 of the membrane potential (a), voltage gated ionic currents (b), Na^+ channel activation (c), Na^+ channel inactivation (d), K^+ channel activation (e), K^+ concentration outside the axon (f), Na^+ concentration outside the axon (g), K^+ concentration inside the axon (h), Na^+ concentration inside the axon (i), and ionic pump currents (j).

the Na^+ and K^+ membrane currents (Fig. 4(b)). Therefore, the small K^+ pump current (Fig. 4(j)) becomes the only current to slowly recover the outside K^+ concentration thereby causing the abrupt change in the reduction rate of outside K^+ concentration. This abrupt change also causes other model parameters to have similar changes.

Application of DC (1.125 mA) to the 10-μm diameter fiber produces an axonal conduction block immediately after generating an initial action potential (Fig. 5(a)). This DC block is caused by a large constant depolarization under the block electrode (at node 20) to about 10 mV from the resting potential -70 mV (Fig. 5(b)). This DC depolarization produces a complete inactivation of the fast Na^+ channel at the block electrode (node

Authorized licensed use limited to: University of Maryland College Park. Downloaded on May 07,2026 at 01:53:45 UTC from IEEE Xplore. Restrictions apply.

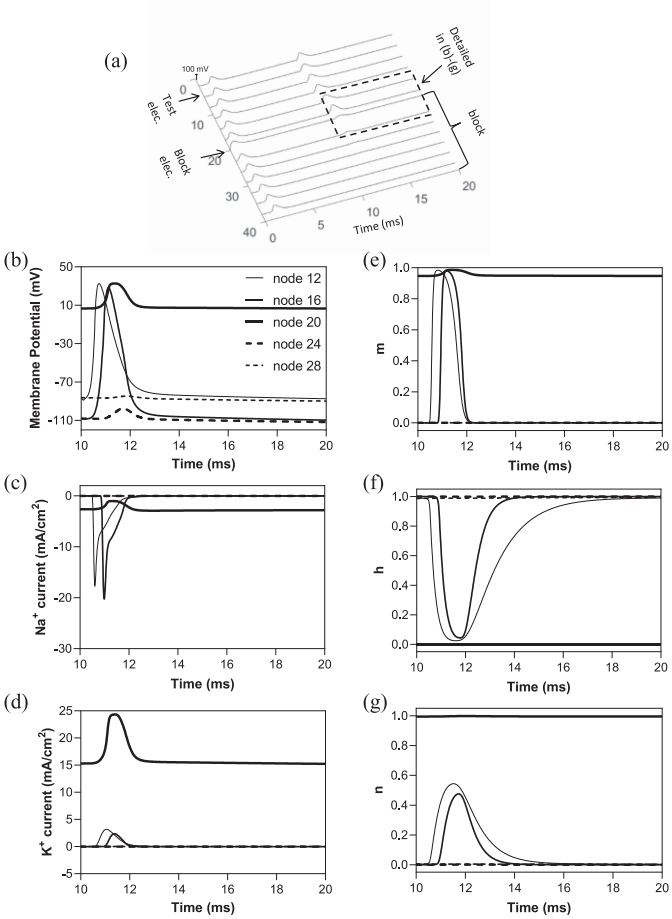

Fig. 5. (a) A DC stimulation of 1.125 mA is applied at node 20 starting at time 0 and results in an initial action potential propagating in two directions. A test pulse (0.5 mA, 0.1 ms) is applied at node 5 at the time of 10 ms and induces an action potential that fails to propagate through the node 20. (b)-(g). Detailed presentations of the membrane potential (b), voltage-gated ionic currents (c), (d), activation and inactivation of Na^+ and K^+ channels (e), (f), (g) at nodes 12, 16, 20, 24, 28 as indicated in (b).

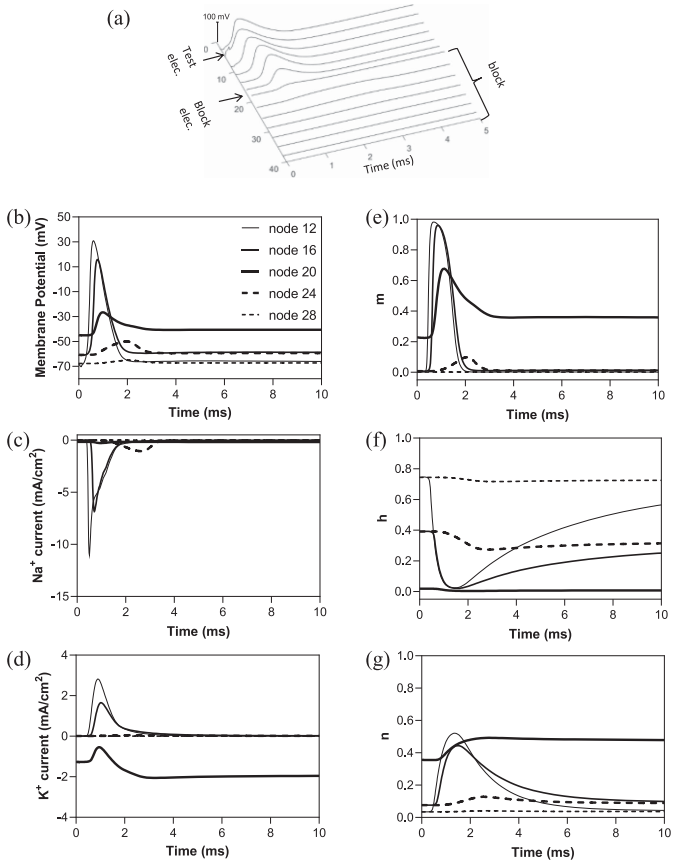

Fig. 6. (a) A test pulse (0.5 mA, 0.1 ms) is applied at node 5 at the time of 31707 ms after turning off the DC stimulation (1.125 mA) that is applied at node 20 for 30 seconds. The resulting action potential fails to propagate through the node 20. (b)-(g). Detailed presentations of the membrane potential (b), ionic currents (c), (d), activation and inactivation of Na^+ and K^+ channels (e), (f), (g) at nodes 12, 16, 20, 24, 28.

20, see Fig. 5(f)), and leaves only a small persistent Na^+ current that is slightly reduced when the action potential arrives at the block electrode (Fig. 5(c)).

After terminating the 30-secs DC stimulation, the axonal conduction block is maintained for about 32 secs as the depolarization is gradually recovering (between the 2 dashed lines in Fig. 4), i.e., a post-stimulation block. Fig. 6(a) shows that the action potential initiated by the test electrode (node 5) at the time of 31.707 secs after termination of the DC stimulation is blocked when it arrives at the block electrode at node 20. This block is due to the depolarization under the block electrode (node 20, Fig. 6(b)) that produces a complete inactivation of the fast Na^+ channel (Fig. 6(f)) preventing the arriving action potential to generate a large inward Na^+ current (Fig. 6(c)). However, the same action potential initiated 1 ms later (at 31.708 secs after termination of the DC stimulation) successfully propagates through the site of the block electrode (Fig. 7(a)), although conduction is significantly delayed at the block electrode due to the depolarization. In fact, there is no action potential generated at the block electrode (Fig. 7(a) and (b)) since the constant depolarization still fully inactivates the fast Na^+ channel (Fig. 7(f)) resulting in a very small Na^+ current when the action potential arrives at the block electrode (node 20, Fig. 7(c)). Therefore, the action potential is blocked at the block electrode. However, axonal conduction is maintained because the action potential jumps over the block electrode by initiating another action potential at the node 24 (Fig. 7(a) and (b)) to continue the propagation albeit with a significant delay.

D. Effect of the Peri-Myelin Space and DC Amplitude on Post-Stimulation Block

The duration of post-stimulation block is influenced by both the volume of the peri-myelin space and the DC amplitude (Fig. 8). With a large peri-myelin space, the same DC produces a short duration post-stimulation block (Fig. 8(a)). When the peri-myelin space thickness increases to 1.25% of the fiber diameter, the duration of post-stimulation block becomes zero, i.e., no post-stimulation block is induced by the 30-secs DC (Fig. 8(a)). With a fixed peri-myelin thickness of 0.5%, the duration of post-stimulation block increases with increasing DC

Authorized licensed use limited to: University of Maryland College Park. Downloaded on May 07,2026 at 01:53:45 UTC from IEEE Xplore. Restrictions apply.

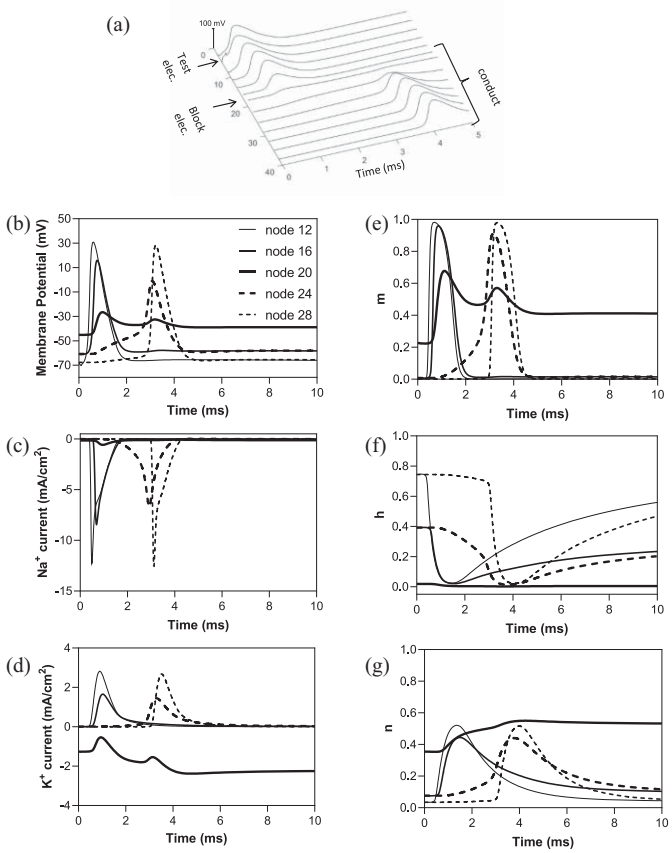

Fig. 7. (a) A test pulse (0.5 mA, 0.1 ma) is applied at node 5 at the time of 31708 ms after turning off the DC stimulation (1.125 mA) that is applied at node 20 for 30 seconds. The resulting action potential successfully propagates through the node 20. (b)-(g). Detailed presentations of the membrane potential (b), ionic currents (c), (d), activation and inactivation of Na^+ and K^+ channels (e), (f), (g) at nodes 12, 16, 20, 24, 28.

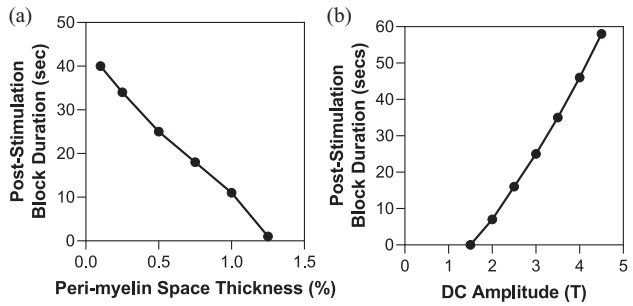

Fig. 8. Post-stimulation block duration decreases with increasing peri-myelin space thickness (a) and increases with increasing DC intensity (b). The post-stimulation block duration is measured after applying DC for 30 seconds on a nerve fiber of 10 μm diameter. (a). The DC intensity is 1.02 mA (3T). (b). The threshold (T) intensity for a DC block is 0.34 mA and the peri-myelin space thickness is 0.5% of the fiber diameter.

amplitude (Fig. 8(b)). If the DC amplitude is too low (1.25 times the DC block threshold T), the 30-secs DC cannot produce a post-stimulation block, i.e., the duration of post-stimulation block becomes zero (Fig. 8(b)).

IV. Discussion

This study established a new axonal conduction model for myelinated axons (Fig. 1) that is different from the classical models [6], [7], [8], [9] by including the changes in intracellular and extracellular ion concentrations and ion pump activity. This new model successfully simulated the generation and propagation of an action potential (Fig. 2), the refractory period (Fig. 3), and both the acute block during DC (Fig. 5) and the post-stimulation block after termination of the DC (Fig. 6). These results validated the model's ability to simulate not only the acute response during the stimulation but also the long-lasting post-stimulation effect caused by changes in ion concentrations as well as the slow recovery of the post-stimulation effect by ion pump activity (Fig. 4).

The conduction velocity for myelinated axons of different fiber diameters (5-15 μm) calculated by the new model agrees very well with the results obtained in animals (Fig. 2(h)) [19]. In addition, the model calculates an absolute refractory period of 2.7 ms and the excitation threshold (T) that recovers to 1.1T at 5 ms during the refractory period (Fig. 3(a)). These results agree well with those obtained from an animal study using myelinated axons from frog sciatic nerve [20] that showed an absolute refractory period of 2.61 ms and a relative refractory period ending at 4 ms. At a high temperature (37°C), the action potential duration is shortened to $<$1 ms [6], which could also shorten the absolute refractory period to $<$1 ms. The maximal firing frequency for a 10-μm diameter fiber is 268 Hz when the axon is stimulated at 2T intensity (Fig. 3(c)). This maximal firing frequency is determined by the relative refractory period of 3.6 ms at 2T (Fig. 3(a)) since the 268 Hz has an inter-pulse interval of 3.7 ms. Animal studies using myelinated axons from frog spinal dorsal roots [21], [22] showed the maximal firing frequency ranging from 200 Hz to 350 Hz. Furthermore, the new model also successfully simulated the acute conduction block occurring during the DC stimulation (Fig. 5). It is well known that axonal conduction can be blocked during the application of DC [23], [24]. This new model reveals the same DC block mechanism as the classical model [25], i.e., the Na^+ channels are completely inactivated during the DC (Fig. 5(c) and (f)). These simulation results verify that the new model is the same as the classical models in predicting the basic axonal responses such as the conduction velocity, the refractory period, the maximal firing frequency, and the acute DC block.

The new model also successfully simulated post-stimulation block (Fig. 6) that the classical axonal conduction model failed to simulate [10]. Post-DC block has been observed in recent animal studies using rat sciatic nerve [4], [5] showing that the block duration increases with the amplitude of the DC, i.e., the total charges delivered by the DC. This observation from animal studies agrees well with our simulation result (Fig. 8(b)) showing that the post-DC block duration is increased as the DC amplitude is increased. Furthermore, our new model reveals that the post-stimulation block is caused by a large depolarization (Fig. 6) that gradually reduces during the post-stimulation block period (Fig. 4(a)). This large post-stimulation depolarization

Authorized licensed use limited to: University of Maryland College Park. Downloaded on May 07,2026 at 01:53:45 UTC from IEEE Xplore. Restrictions apply.

is due to the significant increase in K^+ concentration outside the axonal node (>200 mM in Fig. 4(f)) since the K^+ channel is fully open (Fig. 4(e)) generating a large K^+ current during the DC. After terminating the DC, the reversal of the high K^+ concentration outside the axon (Fig. 4(f)) is mainly driven by ionic diffusion initially due to the large concentration gradient between the outside (>200 mM, Fig. 4) and inside (about 118 mM, Fig. 4(h)). Then, the K^+ pump activity (Fig. 4(j)) gradually restores the axonal membrane back to the resting potential -70 mV (Fig. 4(a)). The Na^+ concentrations both outside and inside the axon are only changed slightly (Fig. 4(g) and (i)) compared to the outside K^+ concentration (Fig. 4(f)) because the DC completely inactivates the fast Na^+ channel during the stimulation (Fig. 4(d)). Therefore, this new model reveals a post-stimulation block that is mainly caused by the large accumulation of K^+ outside the axon.

The post-stimulation duration can be influenced by the volume of the peri-myelin space and the DC amplitude (Fig. 8). Higher DC amplitude will produce a larger K^+ current during the stimulation (Fig. 4(b)) and a larger K^+ accumulation outside the axon at the end of the stimulation (Fig. 4(f)), requiring a longer time to recover, i.e., a longer post-stimulation block period (Fig. 8(b)). Meanwhile, a larger peri-myelin space will reduce the K^+ concentration outside the axon when the same amount of K^+ is moved outside during the DC stimulation (Fig. 4(f)), requiring a shorter time to recover, i.e., a shorter post-stimulation block period (Fig. 8(a)). It is worth noting that if the peri-myelin space is too large (1.25% thickness in Fig. 8(a)) the 30-sec DC at 3T intensity fails to produce a post-stimulation block, i.e., the block duration is zero. Therefore, to induce a post-stimulation block the DC stimulation must be increased in amplitude or duration to move more K^+ outside. Similarly, the outside K^+ accumulation can also be influenced by other factors such as ionic diffusion across the perineurium or glia cell K^+ buffering [26]. These influencing factors are not included in the current model, but they should be included if we want to study the influence of the structural geometry of a compound nerve that consists of many bundles of nerve fibers separated by perineurium or study the glia cell K^+ buffering effect on post-stimulation block. Since our model does show that changing the accumulation rate of the outside K^+ can significantly change the duration of post-stimulation block (Fig. 8), it is possible that the ionic permeability of the perineurium or glia cell K^+ buffering can significantly affect the post-stimulation block.

We used the same concentrations in the thin and long periaxonal space at the axonal node because the ion diffusion in this space is much faster than the ion crossing the small nodal membrane. After the long stimulation duration (30 seconds) the ions that crossed the nodal membrane have diffused almost completely into the entire periaxonal space. In addition, the ion concentrations in the periaxonal space can be changed by many other factors such as the ionic permeability of the perineurium or glia cell K^+ buffering. Therefore, the ion concentrations in the periaxonal space are serving as our model interface that can be used to take account of many other external factors that can influence the accumulation rate of the ions in this space. In this study we used 0.5% of fiber diameter as a possible example for peri-myelin space thickness and analyzed the sensitivity of this parameter (Fig. 8(a)) since the peri-myelin space is variable for different nerves in different species.

This study reveals that the significant increase in K^+ concentration outside the axonal node (>200 mM, Fig. 4(f)) causes the post-DC block because the change in Na^+ concentration inside the axonal node is relatively small (only about 4 mM, Fig. 4(i)). This un-symmetric change in ion concentrations is due to 2 factors. First, the DC stimulation completely inactivates the fast Na^+ channel (Fig. 4(d)) only leaving a small persistent inward Na^+ current during the stimulation (Fig. 4(b)), while it fully opens the K^+ channel (Fig. 4(e)) allowing a large outward K^+ current (Fig. 4(b)). Second, the periaxonal space outside the node is much smaller than the axoplasm space inside the node. For a myelinated axon of 10-μm fiber diameter, the periaxonal space volume at each node is 1885 μm^3 but the axoplasm volume is 42805 μm^3 that includes the nodal segment and the segments under the myelin (2 MYSA segments, 2 FLUT segments, and 6 STIN segments, see Table I). Therefore, with the same ionic diffusion rate along the longitudinal direction of the axon the ion accumulates faster outside the node than inside the node. Myelin plays an important role in creating this un-symmetric ion concentration change because it only allows ion passing through the membrane at the node which represents less than 0.1% of the axon length covered by the myelin between the neighboring axonal nodes (see Table I). Please note that the myelin sheath is modeled as an isolator (capacitor) that is same as the previous study by McIntyre et al. [15]. However, it is a very different situation for unmyelinated axons where the myelin barrier is absent, and the ions can cross the membrane along the entire length of the axon. Therefore, our recent study using an unmyelinated axon model showed that both K^+ accumulation outside the axon and Na^+ accumulation inside the axon could play a role in post-DC block [11], [12].

The new axonal conduction model established in this study successfully simulated the post-stimulation block phenomenon while the classical model based on FH equations [10] without changes in ion concentrations failed to simulate the post-stimulation block. This difference indicates that the changes in intracellular and extracellular ion concentrations play an important role in producing the post-stimulation block. Recent animal studies [27], [28] have shown that post-stimulation block can also be induced by high frequency (kHz) stimulation that has been applied clinically to the spinal cord to treat chronic back pain [29] and used to block peripheral nerves to treat extreme obesity [30] or amputation limb pain [31]. Despite these clinical successes, the mechanism underlying the effects of kHz stimulation on axonal conduction/block is still not fully understood. Thus, the new axonal conduction model developed in this study could be used to further investigate the possible mechanisms underlying the post-stimulation block induced by kHz stimulation.

V. Conclusion

This study established a new axonal conduction model for myelinated axons that includes changes in intracellular and

Authorized licensed use limited to: University of Maryland College Park. Downloaded on May 07,2026 at 01:53:45 UTC from IEEE Xplore. Restrictions apply.

extracellular ion concentrations and ion pump activity. The model not only successfully simulated the initiation, propagation, and block of the action potential as revealed by the classical FH models, but also simulated the post-stimulation block phenomenon that the classical FH model failed to simulate. This new model will be useful for better understanding of the mechanisms underlying long-duration stimulation that changes ion concentrations and triggers ion pump activity.

REFERENCES

[1] A. Ramirez-Zamora and J. L. Ostrem, "Globus pallidus interna or subthalamic nucleus deep brain stimulation for Parkinson disease: A review," *JAMA Neurol.*, vol. 75, no. 3, pp. 367–372, 2018.

[2] P. Verrills et al., "A review of spinal cord stimulation systems for chronic pain," *J. Pain Res.*, vol. 9, pp. 481–492, 2016.

[3] M. Tutolo et al., "Efficacy and safety of sacral and percutaneous tibial neuromodulation in non-neurogenic lower urinary tract dysfunction and chronic pelvic pain: A systematic review of the literature," *Eur. Urol.*, vol. 73, no. 3, pp. 406–418, 2018.

[4] F. Yang et al., "Differential expression of voltage-gated sodium channels in afferent neurons renders selective neural block by ionic direct current," *Sci. Adv.*, vol. 4, no. 4, 2018, Art. no. eaaq1438.

[5] T. L. Vrabec et al., "A carbon slurry separated interface nerve electrode for electrical block of nerve conduction," *IEEE Trans. Neural Syst. Rehabil. Eng.*, vol. 27, no. 5, pp. 836–845, May 2019.

[6] F. Rattay and M. Aberham, "Modeling axon membranes for functional electrical stimulation," *IEEE Trans. Biomed. Eng.*, vol. 40, no. 12, pp. 1201–1209, Dec. 1993.

[7] F. Rattay, "Analysis of models for extracellular fiber stimulation," *IEEE Trans. Biomed. Eng.*, vol. 36, no. 7, pp. 676–682, Jul. 1989.

[8] A. L. Hodgkin and A. F. Huxley, "A quantitative description of membrane current and its application to conduction and excitation in nerve," *J. Physiol.*, vol. 117, no. 4, pp. 500–544, 1952.

[9] B. Frankenhaeuser and A. F. Huxley, "The action potential in the myelinated nerve fibre of Xenopus laevis as computed on the basis of voltage clamp data," *J. Physiol.*, vol. 171, no. 2, pp. 302–315, 1964.

[10] X. Zhang et al., "Mechanism of nerve conduction block induced by high-frequency biphasic electrical currents," *IEEE Trans. Biomed. Eng.*, vol. 53, no. 12, pp. 2445–2454, Dec. 2006.

[11] Y. Zhong et al., "Model analysis of post-stimulation effect on axonal conduction and block," *IEEE Trans. Biomed. Eng.*, vol. 68, no. 10, pp. 2974–2985, Oct. 2021.

[12] Y. Zhong et al., "Mechanisms underlying poststimulation block induced by high-frequency biphasic stimulation," *Neuromodulation*, early access, doi: 10.1111/ner.13501.

[13] L. Joseph and R. J. Butera, "Unmyelinated Aplysia nerves exhibit a nonmonotonic blocking response to high-frequency stimulation," *IEEE Trans. Neural Syst. Rehabil. Eng.*, vol. 17, no. 6, pp. 537–544, Dec. 2009.

[14] N. A. Pelot and W. M. Grill, "In vivo quantification of excitation and kilohertz frequency block of the rat vagus nerve," *J. Neural Eng.*, vol. 17, no. 2, 2020, Art. no. 026005.

[15] C. C. McIntyre et al., "Modeling the excitability of mammalian nerve fibers: Influence of afterpotentials on the recovery cycle," *J. Neurophysiol.*, vol. 87, no. 2, pp. 995–1006, 2002.

[16] W. M. Haynes, *CRC Handbook of Chemistry and Physics*, 97th ed. Boca Raton, FL, USA: CRC press, 2016.

[17] J. Keener and J. Sneyd, *Mathematical Physiology I: Cellular Physiology*, 2nd ed. New York, NY, USA: Springer, 2009.

[18] D. R. Scriven, "Modeling repetitive firing and bursting in a small unmyelinated nerve fiber," *Biophys. J.*, vol. 35, no. 3, pp. 715–730, 1981.

[19] N. A. Hutchinson, "Conduction velocity in myelinated nerve fibres of Xenopus laevis," *J. Physiol.*, vol. 208, no. 2, pp. 279–289, 1970.

[20] S. A. Raymond, "Effects of nerve impulses on threshold of frog sciatic nerve fibres," *J. Physiol.*, vol. 290, no. 2, pp. 273–303, 1979.

[21] S. D. Stoney, "Limitations on impulse conduction at the branch point of afferent axons in frog dorsal root ganglion," *Exp. Brain Res.*, vol. 80, no. 3, pp. 512–524, 1990.

[22] U. Proske and G. J. Stuart, "The initial burst of impulses in responses of toad muscle spindles during stretch," *J. Physiol.*, vol. 368, no. 1, pp. 1–17, 1985.

[23] J. G. Whitwam and C. Kidd, "The use of direct current to cause selective block of large fibers in peripheral nerves," *Brit. J. Anaesth.*, vol. 47, no. 11, pp. 1123–1133, 1975.

[24] M. Sassen and M. Zimmermann, "Differential blocking of myelinated nerve fibers by transient depolarization," *Pflügers Archiv*, vol. 341, no. 3, pp. 179–195, 1973.

[25] C. Tai et al., "Analysis of nerve conduction block induced by direct current," *J. Comput. Neurosci.*, vol. 27, no. 2, pp. 201–210, 2009.

[26] P. Kofuji and E. A. Newman, "Potassium buffering in the central nervous system," *Neuroscience*, vol. 129, no. 4, pp. 1045–1056, 2004.

[27] G. Yang et al., "Post-stimulation block of frog sciatic nerve by high-frequency (kHz) biphasic stimulation," *Med. Biol. Eng. Comput.*, vol. 55, no. 4, pp. 585–593, 2017.

[28] Z. Wang et al., "Poststimulation block of pudendal nerve conduction by high-frequency (kHz) biphasic stimulation in cats," *Neuromodulation*, vol. 23, no. 6, pp. 747–753, 2020.

[29] R. S. Taylor et al., "High-frequency 10-kHz spinal cord stimulation for chronic back and leg pain: Cost-consequence and cost-effectiveness analyses," *Clin. J. Pain*, vol. 36, no. 11, pp. 852–861, 2020.

[30] C. M. Apovian et al., "Two-year outcomes of vagal nerve blocking (vBloc) for the treatment of obesity in the Recharge trial," *Obesity Surg.*, vol. 27, no. 1, pp. 169–176, 2017.

[31] A. Soin et al., "High-frequency electrical nerve block for postamputation pain: A pilot study," *Neuromodulation*, vol. 18, no. 3, pp. 197–206, 2015.

Authorized licensed use limited to: University of Maryland College Park. Downloaded on May 07,2026 at 01:53:45 UTC from IEEE Xplore. Restrictions apply.